

A fitter code for Deep Virtual Compton Scattering and Generalized Parton Distributions

M. Guidal^a

Institut de Physique Nucléaire d'Orsay, 91405 Orsay, France

Received: 17 July 2008

Published online: 4 September 2008 – © Società Italiana di Fisica / Springer-Verlag 2008

Communicated by M. Anselmino

Abstract. We have developed a fitting code based on the leading-twist handbag Deep Virtual Compton Scattering (DVCS) amplitude in order to extract Generalized Parton Distribution (GPD) information from DVCS observables in the valence region. In a first stage, with simulations and pseudo-data, we show that the full GPD information can be recovered from experimental data if enough observables are measured. If only some of these observables are measured, valuable information can still be extracted, with certain observables being particularly sensitive to certain GPDs. In a second stage, we make a practical application of this code to the recent DVCS Jefferson Lab Hall-A data from which we can extract numerical constraints for the two H GPD Compton form factors.

PACS. 13.60.Fz Elastic and Compton scattering – 13.60.Hb Total and inclusive cross-sections (including deep-inelastic processes) – 12.38.Qk Experimental tests

1 Motivation

Generalized Parton Distributions (GPDs) have emerged during the past decade as a powerful concept and tool to study nucleon structure. They describe, among many other aspects, the (correlated) spatial and momentum distributions of the quarks in the nucleon (including polarisation information), its quark-antiquark content, a way to access the orbital momentum of the quarks, etc.

Formally, in short, the GPDs are Fourier transforms of matrix elements in Quantum Chromo-Dynamics (QCD) for light-cone bilocal operators between nucleon states of different momenta. For helicity-conserving quantities in the quark sector, there are four GPDs, H , \tilde{H} , E , \tilde{E} which depend, in leading-order and leading-twist QCD, upon three variables: x , ξ and t . Both x and ξ express the longitudinal momentum fractions of the two quarks of the bilocal operator, while t is the squared four-momentum transfer between the final and initial nucleon. Experimentally, GPDs are most simply accessed through the measurement of exclusive lepton production of a photon (Deep Virtual Compton Scattering —DVCS) and, possibly, of a meson. GPDs are then accessed through the factorization with an elementary perturbative process, which leads to the so-called handbag diagram, predicted to be dominant at small t and large Q^2 , where Q^2 is the virtuality of the initial photon. Figure 1 shows schematically these

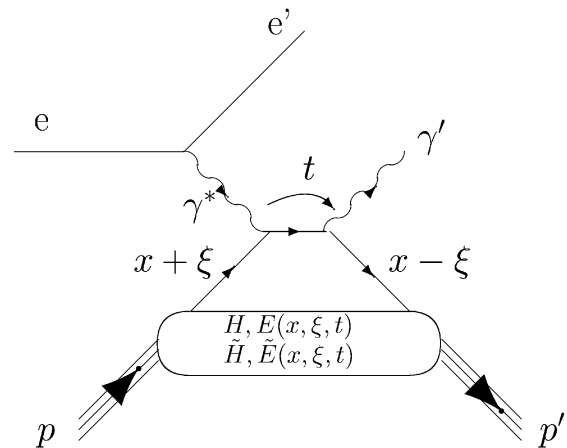


Fig. 1. The handbag diagram for the DVCS process on the proton $ep \rightarrow e'p'\gamma'$. Here $x + \xi$ and $x - \xi$ are the longitudinal momentum fractions of the initial and final quark, respectively, and $t = (p - p')^2$ is the squared momentum transfer between the initial and final protons (or equivalently between the two photons). There is also a crossed diagram which is not shown here.

notions for the DVCS process on the proton on which, as a first step, we will concentrate our work and discussion in this article. Indeed the leading-twist contribution is expected to be the most directly accessible for DVCS and proton targets currently provide (and will also provide in

^a e-mail: guidal@ipno.in2p3.fr

the near future) the richest data set. We refer the reader to refs. [1–7] for the original theoretical articles and recent comprehensive reviews on GPDs for more details on the theoretical formalism of GPDs and DVCS.

Concerning actual data, the field is now rapidly growing. The first data related to DVCS on the proton were the beam spin asymmetries (BSA) which have been published by the HERMES [8] and CLAS [9] Collaborations in 2001. Although the kinematic range over which the data were integrated was large and, to some extent, the actual exclusivity of the reaction could be disputed, these were the first very encouraging signals that the handbag diagram could be accessed, since several theoretical predictions were in relatively good agreement with the data. Then, longitudinally [10] and transversely [11] polarized target spin asymmetries as well as beam charge asymmetries [12] were measured which, though suffering from the same experimental limitations as the BSAs, also confirmed the general theoretical expectations.

With these first encouraging signals found in non-dedicated experiments, a second generation of DVCS experiments has been launched in the past few years, with fully dedicated detectors, *i.e.* high-resolution electromagnetic calorimeters at Jefferson Lab (JLab) to detect the final-state photon and a recoil detector at HERMES to detect the recoil proton. This has resulted in the publication of the first proton DVCS cross-sections (beam-polarized and unpolarized) in the valence region at a few precise kinematical points by the JLab Hall-A Collaboration [13] and several BSAs over a large kinematic range by the JLab Hall-B Collaboration [14]. HERMES results with the recoil detector are now eagerly awaited.

The field looks extremely promising with a series of novel experiments planned, in particular at JLab, aimed at accurately measuring new DVCS observables, including:

- longitudinally polarized target spin asymmetries and cross-sections (along with double-polarization observables) with JLab experiment E05114 [15],
- transversely polarized target spin asymmetries and cross-sections (along with double-polarisation observables) with JLab experiment E08021 [16],
- new precise (unpolarized and beam-polarized) cross-sections at new kinematics with JLab experiments E06003 [18] and E07007 [17].

A similar experimental program in the longer term future is planned with the JLab 12 GeV upgrade, which will cover a larger phase space (see JLab approved experiments E1206114 [19] and E1206119 [20]).

Anticipating this rich harvest of data, one asks the question how to extract the GPD information from them. We recall that the DVCS process is accompanied by the Bethe-Heitler (BH) process, in which the final-state photon is radiated by the incoming or scattered electron and not by the nucleon itself. The BH process, which is not sensitive to GPDs, is experimentally indistinguishable from the DVCS and interferes with it, thus complicating the matter. Considering that the nucleon form factors are well known at small t , the BH process is however precisely calculable theoretically.

Another issue is that the GPDs, which are a function of the three variables x , ξ and t , enter the DVCS amplitude within a convolution integral over x . Therefore, only ξ and t are accessible experimentally (in the Bjorken limit, $\xi = \frac{x_B/2}{1-x_B/2}$ in which x_B is the standard Bjorken variable). Formally, the DVCS amplitude is proportional to: $\int_{-1}^{+1} dx \frac{H(\mp x, \xi, t)}{x \pm \xi \mp i\epsilon} + \dots$ (where the ellipsis stands for similar terms for E , \tilde{H} and \tilde{E}). Decomposing this expression into a real and an imaginary part, we find that the maximum information that can be extracted from the experimental data at a given (ξ, t) point is $H(\pm\xi, \xi, t)$, when measuring an observable sensitive to the imaginary part of the DVCS amplitude, and $\int_{-1}^{+1} dx \frac{H(\mp x, \xi, t)}{x \pm \xi}$, when measuring an observable sensitive to the real part of the DVCS amplitude.

If one reduces the range of x from $\{-1, 1\}$ to $\{0, 1\}$ in the convolutions, there are in principle eight GPD-related quantities that can be extracted:

$$P \int_0^1 dx [H(x, \xi, t) - H(-x, \xi, t)] C^+(x, \xi), \quad (1)$$

$$P \int_0^1 dx [E(x, \xi, t) - E(-x, \xi, t)] C^+(x, \xi), \quad (2)$$

$$P \int_0^1 dx [\tilde{H}(x, \xi, t) + \tilde{H}(-x, \xi, t)] C^-(x, \xi), \quad (3)$$

$$P \int_0^1 dx [\tilde{E}(x, \xi, t) + \tilde{E}(-x, \xi, t)] C^-(x, \xi), \quad (4)$$

$$H(\xi, \xi, t) - H(-\xi, \xi, t), \quad (5)$$

$$E(\xi, \xi, t) - E(-\xi, \xi, t), \quad (6)$$

$$\tilde{H}(\xi, \xi, t) - \tilde{H}(-\xi, \xi, t) \text{ and} \quad (7)$$

$$\tilde{E}(\xi, \xi, t) - \tilde{E}(-\xi, \xi, t) \quad (8)$$

with

$$C^\pm(x, \xi) = \frac{1}{x - \xi} \pm \frac{1}{x + \xi}. \quad (9)$$

We will call these, respectively, in a symbolic notation, $\text{Re}(H)$, $\text{Re}(E)$, $\text{Re}(\tilde{H})$, $\text{Re}(\tilde{E})$, $\text{Im}(H)$, $\text{Im}(E)$, $\text{Im}(\tilde{H})$ and $\text{Im}(\tilde{E})$. These are also often called the Compton Form Factors (CFFs). Note here the absence of $-\pi$ factors in our definition of the $\text{Im}()$ CFFs with respect to ref. [21]. In the following, for convenience and in a very loose way, we will speak of *real-part* CFFs and *imaginary-part* CFFs to designate generically the CFFs defined by eqs. (1)–(4) and by eqs. (5)–(8), respectively and which correspond to the CFFs associated with the real and the imaginary parts of the DVCS amplitudes, respectively. The CFFs can be decomposed into terms for individual quark flavors which, for the proton, yields: $H(\xi, \xi, t) = \frac{4}{9} H^u(\xi, \xi, t) + \frac{1}{9} H^d(\xi, \xi, t)$ and similarly for E , \tilde{H} and \tilde{E} . The quark flavor separation, which we will not tackle in this study, can be carried out by measuring DVCS on a neutron target, which yields a different quark flavor combination. The first measurements of the neutron BSA have been recently published [22].

In summary, given the interference of the BH process, the deconvolution issue regarding x and the large number (8) of independent quantities to be extracted from the

data, it is clearly a non-trivial task to extract the GPDs from the experimental data and, ultimately to map them in the three variables x , ξ , t .

The first stage of any general program of measuring GPDs should certainly be to extract the eight CFFs from the data for a given ξ , t point, in a model-independent way. This would be only the beginning of the program, since the x -dependence would still need to be deconvoluted using in principle a model with adjustable parameters. At this stage, let us mention that there might actually be a couple of ways around this issue: firstly, if the Double-DVCS process, (*i.e.* with a virtual photon in the final state) can be measured, then varying the virtuality of the final-state photon provides an extra lever arm and this allows us to measure the GPDs at each x , ξ , t values (though with some limitations if the final photon is timelike) [23,24]. Secondly, dispersion relations could in principle reduce from eight to five the number of GPD quantities to be extracted, by expressing the real-part CFFs defined by eqs. (1)–(4) in terms of integrals over ξ of the respective imaginary-part CFFs defined by eqs. (5)–(8), plus a real subtraction constant (at fixed ξ and t). This strategy requires one to measure data over a very wide range in ξ (at fixed t) unless one has good reasons to truncate the integral or to extrapolate. We refer the reader to refs. [25–28] for discussions on this subject and, in particular, to ref. [27] for actual fits to the DVCS data in collider kinematics.

As a first approach, in this article, we focus our study on the most general case, in which the eight quantities of eqs. (1)–(8) are independent. Our present purpose is to understand to what extent, given the leading-twist and leading-order QCD DVCS amplitude, the CFFs can be extracted from various observables. We present our work in three steps, corresponding to the next three sections. In the next section, we present the general framework of the fitting code that we have developed. In particular, we present the tests that we have carried out in a Monte Carlo approach using simulated data. With ideal (*i.e.* insignificant) statistical error bars, we will learn general features such as which observable is sensitive to which CFF, what are the highest reconstruction efficiencies that one can expect to achieve in such ideal conditions, etc. In the following section, we will simulate real experimental conditions by introducing a smearing of the simulated data together with realistic error bars. We will then discuss the resulting reconstruction efficiencies and the uncertainties on the reconstructed GPD parameters. Finally, in a last stage, in sect. 4, we will apply our fitting code to the recent JLab Hall-A DVCS data and will attempt to extract quantitatively some of the first real GPD quantities.

2 Monte Carlo study

In this section, we present the general features of our fitter code and, in particular, the way we have tested it and established its reliability and efficiency. Our fitter code is simply based on the merging of the well-established VGG [29,30] code, which calculates numerically, using

model CFFs, the leading-order and leading-twist handbag DVCS + BH amplitudes and observables, and the well-known MINUIT minimization program from CERN [31]. The VGG code uses its own models for the GPDs but in fact any GPD model can be used. For our fitting purposes, the idea is to consider the CFFs that enter the DVCS amplitude as free parameters to be fitted and to see how well they can be extracted from the DVCS data.

We have started by testing and studying our code with pseudo-data. The procedure we have followed is based on a Monte Carlo (MC) approach and can be summarized by the following general steps; for a given experimental kinematic point uniquely defined by E_e , Q^2 , ξ and t (E_e being the electron beam energy):

1. We generate randomly a set of values for the quantities $\text{Re}(H)$, $\text{Re}(E)$, $\text{Re}(\tilde{H})$, $\text{Re}(\tilde{E})$, $\text{Im}(H)$, $\text{Im}(E)$, $\text{Im}(\tilde{H})$ and $\text{Im}(\tilde{E})$.
2. From these values, we calculate various observables which we will detail shortly as a function of ϕ , the azimuthal angle between the leptonic and hadronic planes.
3. We fit with our code these distributions with eight “parameters”, which are meant to correspond to $\text{Re}(H)$, $\text{Re}(E)$, $\text{Re}(\tilde{H})$, $\text{Re}(\tilde{E})$, $\text{Im}(H)$, $\text{Im}(E)$, $\text{Im}(\tilde{H})$ and $\text{Im}(\tilde{E})$.
4. We finally compare the fitted values to the generated ones and draw our conclusions.

This procedure is going to be looped over several hundred times, exploring the whole phase space of values, within given limits, that can be taken by $\text{Re}(H)$, $\text{Re}(E)$, $\text{Re}(\tilde{H})$, $\text{Re}(\tilde{E})$, $\text{Im}(H)$, $\text{Im}(E)$, $\text{Im}(\tilde{H})$ and $\text{Im}(\tilde{E})$. In doing so, we do not make any assumption or do not take into account any information on the absolute or the relative values of the generated GPDs, such as, for example, whether $\text{Im}(H)$ is dominant over $\text{Im}(\tilde{H})$ and $\text{Im}(\tilde{E})$, which could well be the case in reality. In this way, we place ourselves, in the framework of this very general study, in the “blindest”, the least biased and the most conservative of situations. Entering physically motivated information or constraints on the CFFs can of course only improve the results that we obtain. Before presenting the results of our Monte Carlo study, let us mention a few details.

We will consider nine independent observables which can be expected to be measured with relatively good accuracy in the near future. These are: σ , $\Delta\sigma_{z0}$, $\Delta\sigma_{0x}$, $\Delta\sigma_{0y}$, $\Delta\sigma_{0z}$, $\Delta\sigma_{zx}$, $\Delta\sigma_{zy}$, $\Delta\sigma_{zz}$ and $\Delta\sigma_c$. Here σ refers to the unpolarized cross-section. When there are two indices, $\Delta\sigma$ refers to the difference of polarized cross-sections and the two indices refer, respectively, to the polarization of the beam and of the target (*i.e.* $\Delta\sigma_{z0}$ is the difference of cross-sections with a longitudinally polarized beam and an unpolarized target, as has been measured recently by the JLab Hall-A Collaboration [13], and $\Delta\sigma_{zz}$ corresponds to the difference of cross-sections that can be obtained with a longitudinally polarized beam and a longitudinally polarized target). Finally, $\Delta\sigma_c$ refers to the difference of unpolarized cross-sections between a negative and a positive

lepton beam, *i.e.* proportional to the beam charge asymmetry measured by HERMES [12].

Regarding the parameters to be fitted, as a first approach, we have taken into account only seven CFFs, instead of eight: $\text{Re}(H)$, $\text{Re}(E)$, $\text{Re}(\tilde{H})$, $\text{Re}(\tilde{E})$, $\text{Im}(H)$, $\text{Im}(E)$, $\text{Im}(\tilde{H})$, *i.e.* we have set $\text{Im}(\tilde{E})$ to 0. The reason is that the GPD \tilde{E} is usually associated with the pion pole t -channel exchange which is real. Nothing keeps us in principle from considering $\text{Im}(\tilde{E})$ and taking it as an extra free parameter in the fit. However, there is also clearly no need to complicate the fit procedure if it is not justified. Conversely, we have decided to let $\text{Re}(\tilde{E})$ be a free parameter, even though it is supposed to reflect the pion pole and is therefore well constrained. In this way, the conjecture that \tilde{E} comes from the pion pole can be verified. If this conjecture proves false, the whole parametrization of \tilde{E} will clearly have to be revisited including its imaginary contribution. Thus $\text{Im}(\tilde{E}) = 0$ is the only model assumption that we will make in this study.

Also, we have decided to take as fit parameters, not the CFFs of eqs. (1)–(8) themselves, but the deviations with respect to them. This is not an assumption, simply a convention. In other words, we take some (supposedly) realistic reference values for $\text{Re}(H)$, $\text{Re}(E)$, $\text{Re}(\tilde{H})$, $\text{Re}(\tilde{E})$, $\text{Im}(H)$, $\text{Im}(E)$ and $\text{Im}(\tilde{H})$ and fit the coefficients that multiply these reference values to the MC data. Therefore in our MC study, we are going to generate randomly, in a given range, seven real numbers that multiply the seven reference CFFs. From these new (random) CFFs, we generate the DVCS observables. We fit them and our aim is to recover the seven initial multiplicative coefficients, knowing the numerical values of the reference CFFs. We will call these multiplicative coefficients, the GPD multipliers and denote them as $a(\text{Re}(H))$, $a(\text{Re}(E))$, $a(\text{Re}(\tilde{H}))$, $a(\text{Re}(\tilde{E}))$, $a(\text{Im}(H))$, $a(\text{Im}(E))$ and $a(\text{Im}(\tilde{H}))$. Similarly to the CFFs, in the following, for convenience, we will speak of *real-part* and *imaginary-part* multipliers, although, mathematically, all these numbers are obviously real. These can be interpreted as “ratios” of the fitted CFFs to the reference CFFs. Clearly, this is only a matter of convention and instead of these GPD multipliers, we could certainly have generated and fitted $\text{Re}(H)$, $\text{Re}(E)$, etc. directly. Our general motivation is to create the most efficient and robust code by starting the minimization procedure as close as possible to the true solution. This implies that the reference CFFs must be as realistic as possible. For these reference CFFs, we have taken, as a first approach, those given by the VGG parametrization. It is by no means inferred that the VGG parametrization is the most realistic one that currently can be found in the literature, but this was obviously the most convenient choice in our case because they provide a decent description of several existing DVCS experimental data [8,9,14]. However, it is clear that instead of VGG as a reference, any other GPD model could be taken.

In the present study, we have generated seven numbers $a(\text{Re}(H))$, $a(\text{Re}(E))$, $a(\text{Re}(\tilde{H}))$, $a(\text{Re}(\tilde{E}))$, $a(\text{Im}(H))$, $a(\text{Im}(E))$ and $a(\text{Im}(\tilde{H}))$. The range we have considered is $\{-4, 4\}$. This means that we allow the randomly gener-

ated CFFs to vary in absolute value up to a factor 4 from the VGG value. This range $\{-4, 4\}$ is quite arbitrary and does not have any significant impact on the subsequent results of this section. Whether such large variations from the VGG CFFs are realistic or not is not particularly the object of this section which is meant as an exercise, testing the ability to extract GPDs. Let us just mention that the GPDs of the VGG code are normalized and respect the various model-independent relations ($H^q(x, 0, 0) = q(x)$, $\tilde{H}^q(x, 0, 0) = \Delta q(x)$, where $q(x)$ and $\Delta q(x)$ are the unpolarized and polarized parton distributions functions of flavor q , respectively) and sum rules ($\int_{-1}^{+1} dx H^q(x, \xi, t) = F_1^q(t)$, etc.). Although these relations are quite constraining and do not permit a fully arbitrary normalisation of the GPDs, let us note that there are contributions to the GPDs which can escape any formal normalization constraints. For instance, the so-called D -term [32], which cancels at $\xi = 0$ and is odd in x so that it does not contribute to the form factor sum rule, is such a contribution. Also, GPD parametrizations based on other approaches such as in ref. [33] can find in the valence region an H GPD larger by a factor 2 to 3 compared to VGG.

Once the seven initial multipliers are generated, the next step is to calculate with the VGG code the DVCS+BH amplitude and the various (unpolarized, singly polarized, doubly polarized) resulting cross-sections. We recall that, in this study, we restrict ourselves to leading twist. However, in order to ensure gauge invariance of the DVCS amplitude, we mention that the VGG amplitude contains a small (on the order of 10% depending on the kinematics) twist-3 contribution [29,30]. Since Wandura-Wilczek kinematical twist-3 [34] and some other contributions to higher twists are also available in the VGG code (k_\perp effects for instance) [29,30], let us mention that fits can also be done beyond leading twist at the cost of longer computing time.

At given E_e , ξ , Q^2 and t values, we generate the ϕ distributions of the nine observables previously mentioned. Figure 2 shows such distributions calculated from the set of randomly generated $a()$ multipliers which are displayed in table 1. The kinematics correspond to that of the recent JLab Hall-A data [13]: $E_e = 5.75$ GeV, $x_B = 0.36$ (corresponding to $\xi = 0.22$), $Q^2 = 2.3$ GeV² and $-t = 0.28$ GeV². Our goal is therefore to recover the $a()$ values of table 1 from the fit to the ϕ distributions of fig. 2. Once again, we recall that these values are the coefficients that multiply the VGG CFFs, *i.e.* not the CFFs themselves. The corresponding VGG CFFs are also displayed in table 1. The VGG code has several options for the parametrization of the GPDs. As we said, it does not really matter which particular option is used since the VGG CFFs are just meant to be used as starting or reference values and what is ultimately extracted are the deviations from these values. We have used the Regge inspired unfactorized ansatz for the t -dependence [30] of H and E , a factorized t -dependence ansatz for \tilde{H} and the pion pole for the modelling of \tilde{E} . Also, no D -term was used and the parameters $b_{val} = b_{sea} = 1$ in the profile function of the double distributions were selected.

Table 1. One set of seven randomly generated GPD multipliers $a()$, which are used in the illustration of our study, together with the corresponding VGG values for the seven CFFs at $x_B = 0.36$ (corresponding to $\xi = 0.22$), and $-t = 0.28 \text{ GeV}^2$.

	$\text{Re}(H)$	$\text{Re}(E)$	$\text{Re}(\tilde{H})$	$\text{Re}(\tilde{E})$	$\text{Im}(H)$	$\text{Im}(E)$	$\text{Im}(\tilde{H})$
$a()$	0.378	-1.818	3.296	-0.699	-3.732	2.608	-1.285
VGG value	0.658	0.355	0.458	41.705	1.58	0.48	0.43

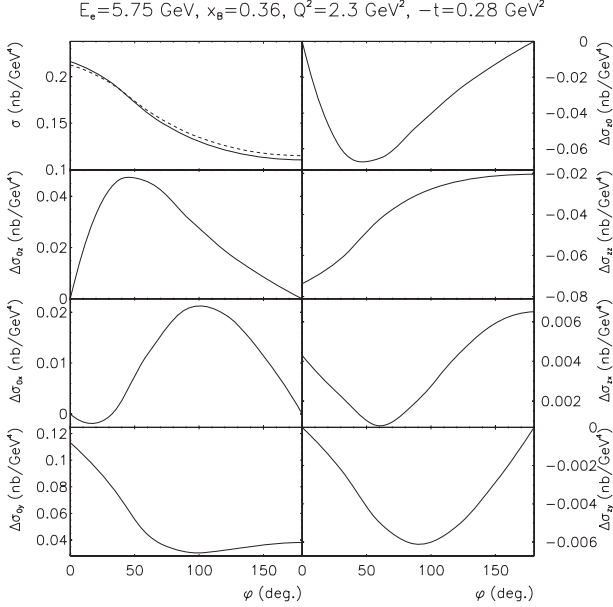


Fig. 2. The nine independent DVCS observables considered in this work as a function of ϕ , at the kinematics $E_e = 5.75 \text{ GeV}$, $x_B = 0.36$, $Q^2 = 2.3 \text{ GeV}^2$ and $-t = 0.28 \text{ GeV}^2$. The curves have been generated with the GPD multipliers of table 1. The left column, from top to bottom, corresponds to the unpolarized cross-section with an electron beam (solid curve) and a positron beam (dashed curve) and the three target single-polarization differences of cross-sections: $\Delta\sigma_{0z}$, $\Delta\sigma_{0x}$ and $\Delta\sigma_{0y}$. The right column, from top to bottom, corresponds to the beam polarized difference of cross-section $\Delta\sigma_{z0}$ and the three beam-target double-polarization differences of cross-sections: $\Delta\sigma_{zz}$, $\Delta\sigma_{zx}$ and $\Delta\sigma_{zy}$. All observables are four-differential in $dx_B dQ^2 dt d\phi$.

Obviously, since the GPD multipliers of table 1 have been randomly generated for our study, they have no particular meaning, and the curves of fig. 2 have no relation to the actual σ and $\Delta\sigma_{z0}$ that the JLab Hall-A Collaboration has measured at similar kinematics.

In this section, we generate the ϕ distributions with “ideal” error bars, *i.e.* 5×10^{-4} in relative value to the cross-sections. The idea is first to gain confidence in our fitting program as well as to understand, under ideal conditions, some general features of the fit procedure such as which GPD is sensitive to which observable, the number of observables needed to extract all GPDs, and so forth. In the following section, we will discuss real conditions by assigning realistic error bars to these distributions.

In fitting these ϕ distributions with the seven free parameters $a(\text{Re}(H))$, $a(\text{Re}(E))$, $a(\text{Re}(\tilde{H}))$, $a(\text{Re}(\tilde{E}))$,

$a(\text{Im}(H))$, $a(\text{Im}(E))$ and $a(\text{Im}(\tilde{H}))$, we stress that we ignore any information that we know about the initial generated values, the idea being to match as much as possible real conditions. In this study, we set the starting values to 0. For real data, as we said, in order to be as close as possible to the true solution, the starting values should be set to 1. The range over which the values of the seven coefficients are allowed to vary is set to $\{-5, 5\}$, *i.e.* somewhat larger than the range of the generated values. This point is essentially the only piece of information that we take from the initial input. We have used a least square method and the MIGRAD minimizer of MINUIT to perform the fit. The quantity that we minimize is thus

$$\chi^2 = \sum_{i=1}^n \frac{(\sigma_i^{theo} - \sigma_i^{exp})^2}{(\delta\sigma_i^{exp})^2}, \quad (10)$$

where σ_{theo} is the theoretical cross-section (or difference of cross-sections) from the VGG code, σ_{exp} is the corresponding (simulated) experimental value (generated from the VGG code as well) and $\delta\sigma_{exp}$ is its associated experimental error bar. We recall that in this section, we consider ideal error bars. The index i runs over the number of observables to be fitted, *i.e.* nine at maximum in the present context. For all the results that we present in the next two sections of this article, fits have been carried out with seven experimental points in ϕ spread in steps of $\phi = 30^\circ$ between 0° and 180° . Little improvement is observed in fitting more ϕ values however, computing time increases. Fitting seven experimental points for each of the nine observables with our seven parameter formulation takes about thirty minutes, running on an average computer. Fitting only σ and $\Delta\sigma_{z0}$ takes less than ten minutes.

We have generated several hundred events in order to have statistically significant results where an event is understood to be a set of seven real values $a(\text{Re}(H))$, $a(\text{Re}(E))$, $a(\text{Re}(\tilde{H}))$, $a(\text{Re}(\tilde{E}))$, $a(\text{Im}(H))$, $a(\text{Im}(E))$ and $a(\text{Im}(\tilde{H}))$. Let us now see how the fitted values of the GPD multipliers compare to the generated ones. We present our results with the support of two figures. In the following, we call a topology a particular combination of some of the nine observables: σ , $\Delta\sigma_{z0}$, $\Delta\sigma_{0x}$, $\Delta\sigma_{0y}$, $\Delta\sigma_{0z}$, $\Delta\sigma_{zx}$, $\Delta\sigma_{zy}$, $\Delta\sigma_{zz}$ and $\Delta\sigma_c$. Figure 3 compares the generated and the reconstructed values of our seven GPD multipliers under different topologies, using one particular event corresponding to the generated GPD multipliers of table 1. Figure 4 summarizes our results for several hundred events, in the phase space $\{-4, 4\}$ of the $a()$ multipliers, for each of the fitted parameters, under the different topologies of fig. 3. The particular event of fig. 3 has been chosen for illustrative purposes because it allows

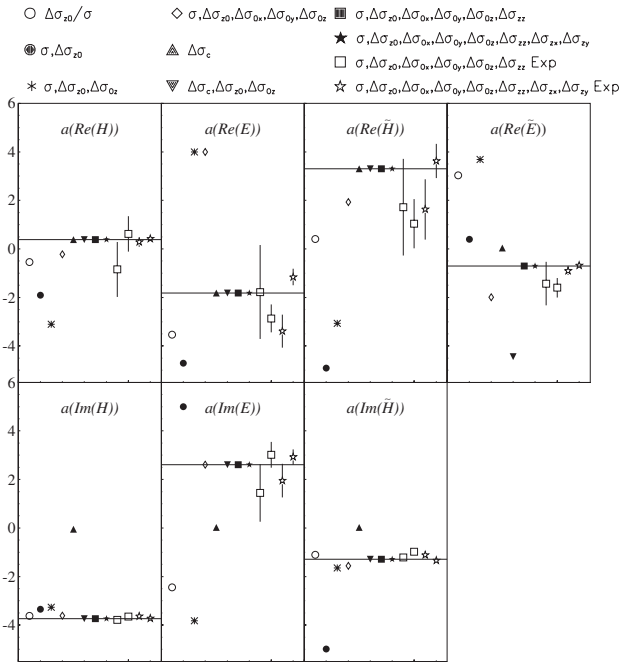


Fig. 3. One particular example of the fit results for different topologies. The solid lines indicate the generated values of the $a()$ GPD multipliers of table 1.

us to make several (not all, though) of the conclusions that we can draw with hundreds of events. Let us start by discussing this figure.

In fig. 3, the solid lines show the (randomly) generated value of the seven multipliers (see table 1), while all the points show the fitted (reconstructed) values obtained from our fitting program, under different topologies. We are going to discuss them one by one, in parallel with fig. 4, to understand if the features that we can infer from fig. 3 are general or simply an accident.

In fig. 3, the empty circles show the reconstructed values obtained if only one observable, the DVCS BSA $\frac{\Delta\sigma_{\neq 0}}{\sigma}$, (which is so far the most widely measured observable) is fitted. We see in this figure that only $a(\text{Im}(H))$ is well reconstructed, as well as $a(\text{Im}(\tilde{H}))$, to a somewhat lesser extent. On very general grounds, it is not at all surprising that fitting only one ϕ distribution, *i.e.* the BSA here, with seven parameters, we are not able to recover all of them. From fig. 4, we see that the good reconstruction of $a(\text{Im}(H))$ is a relatively general feature while the reconstruction of $a(\text{Im}(\tilde{H}))$ is more of a statistical accident. Figure 4 shows, for several hundred randomly generated events, the ratio of the number of well-reconstructed events to the number of generated ones, which we call a reconstruction efficiency, for each GPD multiplier. “Well reconstructed” means that the reconstructed numerical value of a multiplier falls within 5% (dotted curve), 15% (dashed curve) or 25% (solid curve) of the generated value. One learns from this figure that by fitting only the BSA one recovers, at the 25% level, about 55% of the generated values of $a(\text{Im}(H))$ while only $\approx 30\%$ and less than 20% if the reconstructed values are within 15% and 5% of

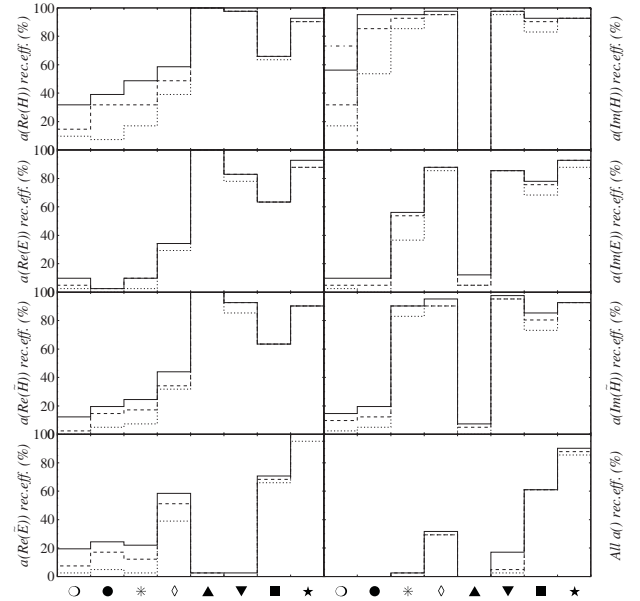


Fig. 4. Reconstruction efficiencies for all the topologies of the seven GPD multipliers and of all of seven in concert. The symbols corresponding to the topologies have been defined in fig. 3. Right bottom plot: reconstruction of all GPD multipliers simultaneously. The reconstruction efficiency is defined as the ratio of the number of well-reconstructed events to the number of generated ones. An event is “well reconstructed” when the reconstructed numerical value matches the generated one to within 5% (dotted curve), 15% (dashed curve) or 25% (solid curve). The dash-dotted curve for the $\text{Im}(H)$ BSA corresponds to the reconstruction efficiency (at the 15% level) if the starting value for $\text{Im}(H)$ in MINUIT is set to the generated one $\pm 20\%$.

the generated ones, respectively (first column of the upper right plot of fig. 4). Once again, the efficiencies for recovering $a(\text{Im}(H))$ are calculated with all $a()$'s in the range $\{-4, 4\}$. Therefore, if $a(\text{Im}(H))$ happens to be close to zero while the other $a()$'s not, it should not be surprising that $a(\text{Im}(H))$ is not well recovered. If in reality $\text{Im}(H)$ dominates over the other GPDs then these efficiencies can only increase. Therefore, the numbers that we quote for these efficiencies and which are displayed in fig. 4 should be taken with great care because they really depend on the relative value and weight of each CFF. In addition, the kinematics can also change the weight of each CFF. Thus these efficiencies reflect more a “sensitivity” of a given CFF to some observable(s) rather than an absolute efficiency and they have only a general statistical meaning in the present context.

Another way to improve the efficiency of the fit is to set the starting values close to the true solution. It will then be less likely that MINUIT falls into some local minimum. For instance, the dash-dotted curve in the first column (*i.e.* the BSA) of the upper right plot (*i.e.* $\text{Im}(H)$) of fig. 4 shows the reconstruction efficiency (at the 15% level) if the starting value in MINUIT for $\text{Im}(H)$ is set to the *generated* $\text{Im}(H)$ (smeared at the 20% level) instead of at 0 as we have done so far. Biasing and guiding the fit in such a way doubles the probability of recovering the original value.

Despite all these caveats, we can still learn a lot from fig. 4. We can note that $a(\text{Im}(\tilde{H}))$ is not recovered more than 15% of the time, which means that the good reconstruction noted in fig. 3 is not generally the case and that the reconstruction of the $\text{Im}(H)$ CFF in this topology is thus very dependent on its particular value and weight with respect to the other CFFs. On the contrary, fig. 4 shows a feature that fig. 3 might not have hinted to, *i.e.* that the BSA has some non-negligible sensitivity to $\text{Re}(H)$ since in $\approx 35\%$ of the cases, it is well reconstructed at the 25% level.

The sensitivity of the BSA to $\text{Im}(H)$ is a well-known feature since it can be shown analytically (see ref. [21] for instance) that $\text{Im}(H)$ is a dominant contribution to the difference of beam polarized cross-sections $\Delta\sigma_{z0}$ which is the numerator of the BSA. The (limited) sensitivity of the BSA to $\text{Re}(H)$ can be understood through its contribution to the denominator of the BSA which is the unpolarized cross-section σ where the real-part CFFs enter.

In fig. 3, the solid circles show the reconstructed values which are obtained for our seven parameters, if now the two observables just discussed, the unpolarized cross-section σ and the difference of beam polarized cross-section $\Delta\sigma_{z0}$, are both used in the fit rather than just their ratio. In fig. 3, we see similar features to the previous case where only the BSA was fitted, *i.e.* that only $a(\text{Im}(H))$ is fairly well recovered: -3.354 reconstructed against -3.732 generated (table 1). It also confirms that the good reconstruction of $a(\text{Im}(\tilde{H}))$ in the case of the BSA was more an accident than a solid feature. However, the advantage of fitting simultaneously these two observables instead of simply their ratio is shown well in fig. 4 where we see that the reconstruction efficiency of $a(\text{Im}(H))$ now reaches more than 85% (at the 15% precision level) while it was less than 35% in the BSA topology. This illustrates the strong correlation between $\Delta\sigma_{z0}$ and $\text{Im}(H)$ and that $\text{Im}(H)$ can be recovered, through this topology essentially independently of the values of the other GPDs. This conclusion that $\Delta\sigma_{z0}$ is mostly sensitive to $\text{Im}(H)$ and barely to the other GPDs is not new and was already pointed out for instance in ref. [21] analytically. We confirm this numerically.

The topology marked with an asterisk in fig. 3 is the result of the fit when adding one more observable. In addition to the unpolarized cross-section σ and the difference of beam polarized cross-section $\Delta\sigma_{z0}$, we now also fit the difference of longitudinally polarized target cross-sections $\Delta\sigma_{0z}$. One sees in fig. 3 that the four real-part CFFs are as poorly reconstructed as in the previous cases. However, now there is a second imaginary-part CFF, besides $a(\text{Im}(H))$, that is well recovered: $a(\text{Im}(\tilde{H})) = -1.009$ in the fit compared to the generated value -1.285 (table 1). We see from fig. 4 that this conclusion, *i.e.* the strong sensitivity of $\Delta\sigma_{0z}$ to $\text{Im}(\tilde{H})$, which was also already pointed out in ref. [21], is very general. In more than 80% of the cases, $a(\text{Im}(\tilde{H}))$ is well reconstructed in this topology. We also note that the precision on $a(\text{Im}(H))$ is significantly improved. The reconstruction efficiencies corresponding to the 5% (dotted curve) and 15% (dashed curve) criteria

have increased up to $\approx 80\%$ (compared to $\approx 50\%$ in the previous topology for the dashed curve).

We now bring two more observables into the fit, *i.e.* the difference of cross-sections obtained with the transverse x and y transverse polarizations of the target. The corresponding results are shown by the open diamonds in fig. 3. We observe that the three imaginary-part CFFs are now well reconstructed and that this conclusion remains true generally. Figure 4 shows that in more than 80% of the cases, $a(\text{Im}(H))$, $a(\text{Im}(\tilde{H}))$ and $a(\text{Im}(E))$ are well reconstructed in this topology. We can thus infer that the target transverse (single) polarisation observables are very sensitive to $\text{Im}(E)$ and that measuring the five observables σ , $\Delta\sigma_{z0}$, $\Delta\sigma_{0x}$, $\Delta\sigma_{0y}$, and $\Delta\sigma_{0z}$ allows us to extract the three imaginary-part CFFs reliably. Furthermore, fig. 4 shows that, although it is not illustrated particularly well by fig. 3, the combination of these five observables has a significant sensitivity to the four real-part multipliers. About 40% of them are reconstructed well.

Next, the upright solid triangles show the results of fitting *only* the beam charge difference of cross-sections (*i.e.* no polarization observables). We see now that the three real-part multipliers $a(\text{Re}(H))$, $a(\text{Re}(E))$, $a(\text{Re}(\tilde{H}))$ are reconstructed well while no imaginary-part multiplier is recovered at all. Figure 4 confirms that this is the case at basically the 100% level (the few well-reconstructed imaginary-part multipliers in this topology in fig. 4 are clearly accidental). Because, on general grounds, $\Delta\sigma_c$ is expected to be sensitive only to the real part of the DVCS amplitude, this result comes as no surprise. We also note in fig. 3 that the real-part multiplier $a(\text{Re}(\tilde{E}))$ is not reconstructed in this topology. This is a general feature since, as seen from fig. 4, $a(\text{Re}(\tilde{E}))$ is not reconstructed in any of the cases with our high statistics event sample. Again, the couple of percent of events well reconstructed clearly result by coincidence. This feature can be demonstrated analytically by the same kind of argument used to show that the difference of beam polarized cross-sections $\Delta\sigma_{z0}$ is insensitive to $\text{Im}(\tilde{E})$.

In fig. 3, the upside-down solid triangles show the effect of fitting $\Delta\sigma_{z0}$ and $\Delta\sigma_{0z}$, in addition to $\Delta\sigma_c$. Now, in addition to the three real-part multipliers $a(\text{Re}(H))$, $a(\text{Re}(E))$, $a(\text{Re}(\tilde{H}))$, the three imaginary-part multipliers are well reconstructed following our previous discussions. We note that there is a slight decrease of the reconstruction efficiency of the three real-part multipliers when fitting simultaneously $\Delta\sigma_c$, $\Delta\sigma_{z0}$ and $\Delta\sigma_{0z}$ compared to fitting only $\Delta\sigma_c$. This is due to the fact that, here, we have minimized the sum of the three χ^2 's corresponding to the minimization of $\Delta\sigma_c$, $\Delta\sigma_{z0}$ and $\Delta\sigma_{0z}$, and it can be shown that the derivatives with respect to the imaginary-part CFFs are the highest compared to those with respect to the real-part CFFs. In other words, in doing so, one loses some sensitivity to the real-part CFFs. Therefore, in such a situation, where a set of observables is sensitive only to some other independent CFFs, like $\Delta\sigma_c$ to the real-part CFFs, and another set of observables only to some other independent CFFs, like $\Delta\sigma_{z0}$ and $\Delta\sigma_{0z}$ to the imaginary-part CFFs, instead of fitting simultaneously both sets, one

should obviously adopt a two-step procedure and fit independently each set of observables. To illustrate this trivial effect, we leave in fig. 4 the results of our simultaneous fit, with the understanding that in this topology, if we had fitted separately $\Delta\sigma_c$, we would have recovered the same efficiencies than for the upright-solid-triangle topology for the real-part CFFs. This being said, we then see that six of the seven GPD multipliers can be reconstructed in a very economical way by measuring only three observables, and in particular, that the gold-plated way to access the real-part CFFs is with the beam charge difference of cross-sections.

However, the next symbol (solid square) in fig. 3 shows that there is another way of accessing the real-part multipliers with high efficiency. The solid-square topology contains the double-polarization observable $\Delta\sigma_{zz}$ in addition to the open-diamond topology, which was made up of the unpolarized cross-section and the four single-beam or target polarization observables. We then see that all real-part multipliers (in particular including $a(\text{Re}(\tilde{E}))$, to which $\Delta\sigma_c$ was insensitive) and imaginary-part multipliers are well recovered. Figure 4 confirms that the particular event of fig. 3 is not an accident and that these conclusions can be generalized. In about 80% of the cases, the imaginary-part multipliers are well reconstructed at the 25% level, similarly for higher precisions, and in more than 65% of the cases for the real-part multipliers.

The solid stars show the results obtained when fitting all polarization observables simultaneously, *i.e.* now adding the two remaining double-polarization observables $\Delta\sigma_{zx}$ and $\Delta\sigma_{zy}$ to the previous topology. We see from fig. 3 that all seven parameters are well reconstructed, as in the previous topology, but fig. 4 shows that this is now at a higher efficiency which reaches $\approx 90\%$ for all seven multipliers. Fitting eight observables with seven parameters overconstraints the fit, with redundant information, and therefore significantly improves the efficiency.

The remaining symbols in fig. 3 will be discussed in the next section. So far, we have described the general features of our fitting program in the ideal situation, *i.e.* with perfectly precise data, and have demonstrated its general reliability and power to recover all of our seven arbitrary randomly generated parameters (CFFs) from fits to the ϕ distributions, given enough observables. We learned which observables are sensitive to particular CFFs and that, if only some of these observables are available, we could still extract some specific CFF. In particular, one can access in principle the real-part CFFs with relatively high efficiency using double-polarisation observables in addition to beam charge differences.

We now turn to realistic conditions. Ultimately, this program has to be used on real data with finite precision. In the next section, we therefore simulate real experimental conditions and find how robust and reliable the program remains.

3 A more realistic study

We are now going to simulate realistic pseudo-data by assigning experimental error bars to the data to be fit. The

procedure consists not only in assigning an error bar to the simulated ϕ data points but also in smearing the central value according to a Gaussian probability distribution whose standard deviation is equal to the error bar.

Inspired from refs. [13,18], we will assign, at all ϕ 's, a 3.5% error bar to the unpolarized cross-section. For all the differences of cross-sections, we will consider two cases: 10% or 5%, the former being approximatively the error bar on $\Delta\sigma_{z0}$ which is quoted in refs. [13,18] and the latter being a slightly more challenging experimental goal.

We return to fig. 3. The open-square and open-star symbols show the result of the two last topologies discussed in sect. 2 (*i.e.* the solid square and solid stars) when realistic error bars are applied to the pseudo-data in the ϕ distributions. In each of the seven plots, there are two open squares and two open stars. The leftmost, for both symbols, is the result of the fits when the differences of cross-sections are smeared by 10% and the rightmost when they are smeared by 5%. This can clearly be inferred from the size of the error bar of the fitted parameters which is systematically smaller when the data are smeared by 5% compared to 10%. The uncertainties on the fitted parameters that are presented here are the quadratic errors from MINUIT, which is sufficient in the present context where we are looking at statistical effects. However, we will see in the next section when fitting the JLab Hall-A σ and $\Delta\sigma_{z0}$ real data that the error determination requires a more dedicated study, especially when dealing with a underdetermined problem with more parameters to fit than available observables.

We see in fig. 3, for this particular event, that the general conclusions that we reached in the previous section remain, *i.e.* that essentially all seven GPD multipliers are relatively well recovered when fitting the six observables σ , $\Delta\sigma_{z0}$, $\Delta\sigma_{0x}$, $\Delta\sigma_{0y}$, $\Delta\sigma_{0z}$ and $\Delta\sigma_{zz}$ (open-square topology) and eight observables with $\Delta\sigma_{zx}$ and $\Delta\sigma_{zy}$ in addition (open-star topology). However, while in the previous section, the original central values were recovered almost perfectly in most of the cases, there is now a clear dispersion of the reconstructed central values with respect to the generated central ones. We note that this difference is always within two standard deviations and therefore that the errors estimation provided by MINUIT seems very reasonable.

Figure 5 confirms this conclusion with a larger sample (though limited in the display in order not to overcrowd the figure) of events where we observe that for basically all open-stars events (with 10% error bar for the pseudo-data) the difference between the generated and reconstructed values $\Delta a()$ is within three $\sigma_{a()}$'s, with $\sigma_{a()}$ being the MINUIT uncertainty previously discussed. The few cases where it is not the case can easily be identified after inspection; either the χ^2 of the corresponding fit is very bad or the reconstructed (or the generated) value is close to 0, meaning that the observables had very little sensitivity to it.

Figure 5 also shows the solid circles resulting from fits of only σ and $\Delta\sigma_{z0}$. We note that these symbols are visible essentially only in the $\text{Re}(H)$ and $\text{Im}(H)$ plots. This

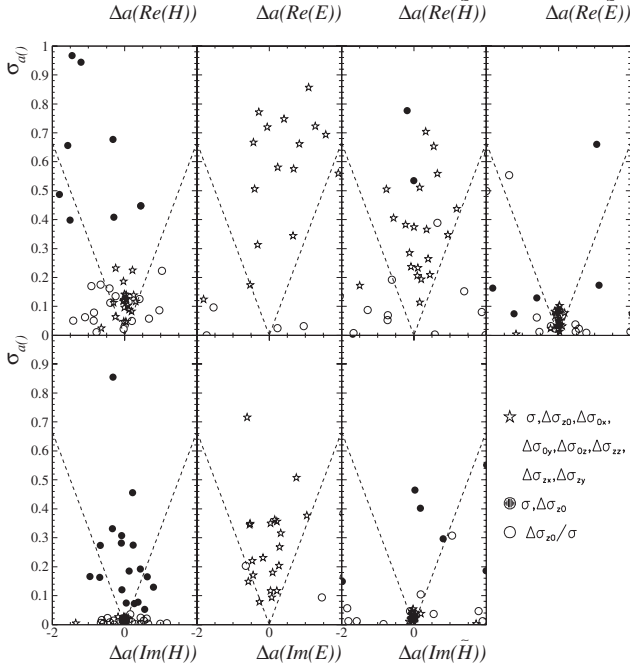


Fig. 5. Uncertainty on the fitted parameters ($\sigma_{a(i)}$), as given by MINUIT, as a function of the difference between the fitted and generated values, for the open-star (with 10% error bar for the pseudo-data), solid-circle and open-circle topologies. The dashed line indicates the three $\sigma_{a(i)}$ limits.

confirms the observations that we made in the previous section that this topology is sensitive to only these two GPD quantities (predominantly $\text{Im}(H)$). Indeed, the absence of solid circles on the other plots means that their uncertainty $\sigma_{a(i)}$ is off-scale, indicating the total lack of sensitivity of this topology to these GPD quantities. For this topology, we also observe the larger $\sigma_{a(i)}$ values in average for $\text{Re}(H)$ than for $\text{Im}(H)$ giving evidence for the stronger sensitivity of the solid-circle topology to $\text{Im}(H)$.

For the open-star topology, the very small $\sigma_{a(i)}$ values that one can observe for the $a(\text{Im}(H))$, $a(\text{Im}(\tilde{H}))$, $a(\text{Re}(\tilde{E}))$ multipliers, compared to the $a(\text{Re}(H))$, $a(\text{Re}(E))$, $a(\text{Re}(\tilde{H}))$ and $a(\text{Im}(E))$ multipliers reflect their very high reconstruction efficiency and reliability. This is confirmed by fig. 6 which shows for the open-star topology, the reconstruction efficiencies of each GPD multiplier. The three GPD multipliers just outlined have clearly the highest reconstruction efficiencies. Comparing the open stars of fig. 6 to the solid stars of fig. 4, we note a loss of reconstruction efficiency when realistic simulated data are fitted, which is particularly important for $\text{Im}(E)$ and $\text{Re}(E)$. For these two GPD multipliers, the reconstruction efficiency is smaller by a factor of 2 or more.

In fig. 5, the open-circle symbols (*i.e.* the fit to only $\Delta\sigma_{z0}$) show up essentially only in the $\text{Re}(H)$ and $\text{Im}(H)$ plots. However, the difference with the solid-circle topology (*i.e.* the fit to σ and $\Delta\sigma_{z0}$ separately) is that most of the points are now NOT within the three $\sigma_{a(i)}$ bands, in spite of the relatively small $\sigma_{a(i)}$ values. This can lead

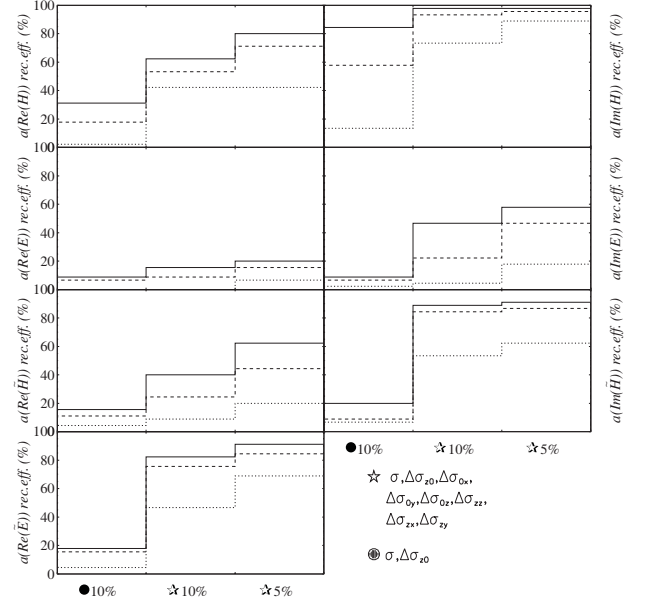


Fig. 6. Reconstruction efficiencies of three “experimental” topologies for the seven GPD multipliers. Left: efficiency of the fit of σ and $\Delta\sigma_{z0}$ with the experimental ϕ distributions being smeared by 3.5% for σ and 10% for $\Delta\sigma_{z0}$. Center: efficiency of the fit of σ , $\Delta\sigma_{z0}$, $\Delta\sigma_{0x}$, $\Delta\sigma_{0y}$, $\Delta\sigma_{0z}$, $\Delta\sigma_{zx}$, $\Delta\sigma_{zy}$ and $\Delta\sigma_{zz}$ with the experimental ϕ distributions being smeared by 3.5% for σ and 10% for all the differences of cross-sections. Right: same as center but with the differences of cross-sections being smeared by 5%. The dotted histograms correspond to a reconstruction efficiency within 5%, the dashed ones within 15% and the solid ones within 25%.

to dangerous interpretations where we might believe that the fitted value of, say $\text{Im}(H)$, are extracted with high precision because of the small $\sigma_{a(i)}$ while the value is not necessarily reliable. Firstly, this suggests that a detailed and dedicated error analysis must be done when dealing with underdetermined systems such as this one where one fits only one observable by seven parameters. We will detail this in the next section. Secondly, let us emphasize that this in no way means that BSAs are dangerous or not useful, but that either they should be complemented by some other observables that provide additional constraints or that some physics input (such as the dominance of H over the other GPDs) must guide the fitting procedure. We recall that we have blinded ourselves, in this study, by not telling the fit which values it should start with.

Let us also note in fig. 3 that the error bars of the open-star topology are always smaller than the ones from the open squares, which is consistent with the fact that fitting eight observables rather than six improves the quality of the fit. Making a blunt generalization from this particular event, one can also conclude that it is almost equivalent to fit eight observables with a precision of 10% (left, open stars) as to fit six observables with a precision of 5% (right, open squares).

In this section, we have simulated real experimental conditions by (Gaussian-)smearing, with a standard deviation equal to realistic experimental error bars, the

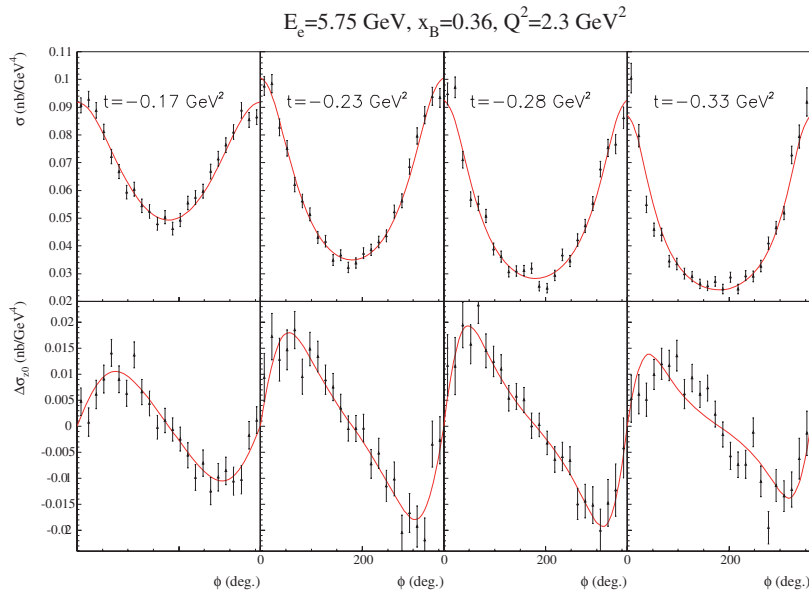


Fig. 7. Top row: DVCS σ , and bottom row: DVCS $\Delta\sigma_{z0}$ as a function of ϕ , at $x_B = 0.36$ and $Q^2 = 2.3 \text{ GeV}^2$ for four different t values. The data are from the JLab Hall-A Collaboration [13]. The curves are the results of the fit from our code to the σ and $\Delta\sigma_{z0}$ observables. The fitted GPD multipliers which produce these curves are displayed in table 2.

observables that we fit with our code. We conclude that the fitting procedure is still very reliable, though somewhat less efficient (with the E CFFs suffering the most important loss of reconstruction efficiency) and that the general conclusions that we drew in sect. 2 remain valid. Having gained confidence in our code and fitting procedure through these simulations with pseudo-data, we now proceed in the next section by applying the code to some real data.

4 Application

The JLab Hall-A Collaboration has recently measured σ and $\Delta\sigma_{z0}$ [13] at $x_B = 0.36$ and $Q^2 = 2.3 \text{ GeV}^2$ for four different t values. From the previous sections, we have learned that the simultaneous fit of these two observables allows us to access $\text{Im}(H)$ at a relatively high efficiency level and to a somewhat lesser extent a few other CFFs such as $\text{Re}(H)$.

We have therefore run our fitting code using the JLab Hall-A data. Figure 7 shows our results. The numerical results of the fit for each GPD multiplier are displayed in table 2.

Several issues are to be discussed concerning this table. Let us start with the uncertainties on the fitted parameters. In the previous section, the uncertainties quoted were the standard quadratic errors from MINUIT, *i.e.* estimated from the second derivative of the χ^2 -function to be minimized with respect to the parameter under consideration, based on the assumption that the χ^2 -function is parabolic near its minimum. This was sufficient for our general purpose of statistically estimating global reconstruction efficiencies and general features of our code. Now, in the present case with real data, the determination of the uncertainty on the fitted parameters has to be

refined. Indeed, we are facing a multidimensional problem (seven parameters to fit) which 1) is non-linear, 2) has potentially strong correlations between the parameters and 3) is severely underconstrained with only two observables to fit seven CFFs. Therefore, a careful and detailed error analysis was carried out with the MINOS subpackage of MINUIT which allows us to explore in a gradual and automated way the χ^2 landscape around the minimum and define one-standard-deviation uncertainties for each parameter when it reaches $\chi^2 + 1$. This method, which is essential for non-linear problems, yields asymmetric error bars. These are presented with the symbols $\sigma_{a()^-}$ and $\sigma_{a()^+}$ (the negative and positive errors, respectively) in table 2. The price one pays is that MINOS is very time-consuming and that the error bar determination of our seven parameters took several hours of computing time.

In table 2, the symbol ∞ means that the uncertainty coming out of MINOS is very large, *i.e.* exceeding the limits given in MINOS. To be precise, the results in table 2 have been obtained by setting, like in the previous section, the lower and upper limits of the domain of variation allowed for the seven parameters to -5 and 5 , respectively. The ∞ symbol means that $\chi^2 + 1$ was never reached in the interval considered. It can be interpreted as a whole range of values for the associated parameter can accommodate the fit with relatively equally good χ^2 . In other words, the corresponding GPD multiplier (or equivalently CFF) is essentially unconstrained and therefore no particular confidence and meaning can be given to the quoted numerical value. This does not mean that the values associated with an ∞ uncertainty in table 2 can take any value, irrespective of the other multipliers. Many of the seven parameters are highly correlated with other parameters and changing the value of one parameter will change the values of others. This means that for those parameters

Table 2. Fitted GPD multipliers $a()$ and their negative ($\sigma_{a()^-}$) and positive ($\sigma_{a()^+}$) uncertainties resulting from the fit of the JLab Hall-A σ and $\Delta\sigma_{z0}$ observables. The χ^2/N_{dof} value for these fits is presented in the rightmost column. As explained in the text, only central values with finite negative and positive uncertainties have a reliable meaning.

		Re(H)	Re(E)	Re(\tilde{H})	Re(\tilde{E})	Im(H)	Im(E)	Im(\tilde{H})	χ^2/N_{dof}
$t = -0.17 \text{ GeV}^2$	$a()$	-5.00	-5.00	-2.58	-0.55	1.11	-4.57	-0.44	1.01
	$\sigma_{a()^-}$	∞	∞	-1.17	-2.45	-0.94	∞	-2.71	
	$\sigma_{a()^+}$	∞	∞	∞	∞	0.18	∞	∞	
$t = -0.23 \text{ GeV}^2$	$a()$	0.22	-5.00	-5.00	-2.07	1.17	-2.61	-0.89	0.92
	$\sigma_{a()^-}$	-1.03	∞	∞	-1.55	-0.98	∞	-2.46	
	$\sigma_{a()^+}$	4.52	∞	∞	4.02	0.17	∞	∞	
$t = -0.28 \text{ GeV}^2$	$a()$	1.64	-5.00	-5.00	-0.92	1.27	-1.15	-1.26	1.44
	$\sigma_{a()^-}$	-0.81	∞	∞	-2.52	-0.97	∞	-1.75	
	$\sigma_{a()^+}$	2.66	∞	∞	1.92	0.10	∞	∞	
$t = -0.33 \text{ GeV}^2$	$a()$	3.82	5.00	5.00	0.87	1.26	-4.00	-2.36	2.31
	$\sigma_{a()^-}$	-0.64	∞	-2.81	-2.36	-0.28	∞	-1.5	
	$\sigma_{a()^+}$	0.63	∞	∞	2.36	0.04	∞	2.18	

with an ∞ uncertainty, the solution is not unique and that other sets of values are also possible. For instance, fixing some GPD multipliers to particular values 0, or 1 (the associated CFF takes its VGG value in this latter case) and letting all other parameters remain free can result in fits with an almost equivalent χ^2 compared to letting all seven parameters free.

However, what is remarkable is that even though many CFFs have an ∞ uncertainty in table 2, a few of them, depending on their t values, come out with finite error bars. For instance, a central value with finite negative and positive uncertainties can be extracted for $a(\text{Im}(H))$ at all t values and for $a(\text{Re}(H))$ at the largest three t values. For these multipliers, the uncertainties, while finite, can be very large, the negative errors ranging from more than 100% at the smallest t values to $\approx 20\%$ at the largest t values. This should not come as a surprise, given the complexity and the underdetermination of our problem. Therefore, the large uncertainties that we obtain do not reflect a lack of quality or precision of the experimental data but rather a lack of constraints and of sensitivity of the observables to certain parameters. In these conditions, it is already a significant success to be able to pull out some reliable and stable information from such partial inputs. We restate that in this study we have left all seven GPD multipliers (or equivalently CFFs) free. If some of them can be fixed, neglected or constrained to a domain smaller than $\{-5, 5\}$, it is clear that these uncertainties can drastically be reduced. This will be the subject of another forthcoming article. We recall that when enough experimental observables are available to fit, as we have shown in the previous sections with simulations, such assumptions will not be necessary and all parameters should be uniquely determined.

We have carried out many checks to get confidence in the numbers (central values and error bars) associ-

ated with finite uncertainties in table 2. For instance, to start the minimization, MINUIT requires us to set some starting values for the parameters to be fitted. As we mentioned in the previous sections, our strategy is in general to set them to the VGG values in order to be, hopefully, close to the true solution. However, we checked that by starting with randomly generated starting values, MINUIT+MINOS were always converging towards the same central values given in table 2 and producing the same corresponding uncertainties at the few percent level.

Another check was to vary the limits of the domain of variation of the parameters (initially set to $\{-5, 5\}$). We made the fits with the domains $\{-3, 3\}$ and $\{-7, 7\}$. The outcome was that, although all central values associated with ∞ uncertainties in table 2 could be different, the few values associated with finite positive and negative uncertainties (*i.e.* $a(\text{Im}(H))$ and $a(\text{Re}(H))$) were found remarkably stable at the few percent level. It was interesting to note that for the two intermediate t values $a(\text{Re}(E))$ and $a(\text{Re}(\tilde{H}))$ would systematically take the lower limit of the domain (*i.e.* -3 or -7 , similarly to the -5 in table 2) though this had no effect on the central values of $a(\text{Im}(H))$ and $a(\text{Re}(H))$. However, a (moderate) effect was found for the uncertainties of $a(\text{Im}(H))$ and $a(\text{Re}(H))$. It was observed that their uncertainties, calculated by MINOS, were slowly increasing as the limits of the domain of variation increased. This can certainly be attributed to the fact that the correlations between the “stable” $a(\text{Im}(H))$ and $a(\text{Re}(H))$ multipliers on the one hand and the “unstable” $a(\text{Re}(E))$ and $a(\text{Re}(\tilde{H}))$ are not completely absent, and that larger (absolute) values of the latter multipliers (since they actually reach the limits of the domain of variation as mentioned earlier) can certainly tend to increase the error bars of the former ones. A few paragraphs below, we make a quantitative comparison of this (moderate) effect.

Table 3. The reference VGG CFFs at $\xi = 0.22$ for the four JLab Hall-A t values. The multiplication of these reference VGG values by the fitted GPD multipliers of table 2 (and their associated error) yield the measured CFFs.

	Re(H)	Re(E)	Re(\tilde{H})	Re(\tilde{E})	Im(H)	Im(E)	Im(\tilde{H})
$t = -0.17 \text{ GeV}^2$	0.25	0.47	0.55	37.71	1.96	0.62	0.51
$t = -0.23 \text{ GeV}^2$	0.49	0.40	0.50	26.91	1.74	0.54	0.46
$t = -0.28 \text{ GeV}^2$	0.66	0.35	0.46	21.71	1.58	0.48	0.43
$t = -0.33 \text{ GeV}^2$	0.78	0.31	0.42	18.16	1.44	0.43	0.40

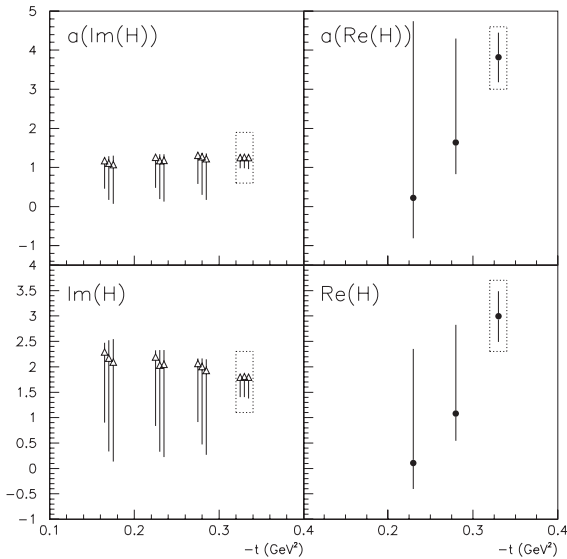


Fig. 8. Upper plots: the $a(\text{Im}(H))$ (left) and $a(\text{Re}(H))$ (right) GPD multipliers as a function of t extracted from the fits of the JLab Hall-A data (fig. 7) at $\xi = 0.22$. Lower plots: the resulting $\text{Im}(H)$ (left) and $\text{Re}(H)$ (right) CFF values. For $a(\text{Im}(H))$ and $\text{Im}(H)$, three results for each t are presented corresponding to fits with the domains of variations $\{-3, 3\}$, $\{-5, 5\}$ and $\{-7, 7\}$ from left to right, respectively. The dotted boxes around the largest t results indicate that the associated fit has a χ^2 about a factor 2 worse (see table 2) than the fits at the other t values.

Although the uncertainties on the $a(\text{Im}(H))$ and $a(\text{Re}(H))$ are rather large, we can notice a few trends. $a(\text{Im}(H))$ is always consistent with 1 within error bars and it tends to increase with t . Although the purpose of this study is not at all to prove (or disprove) the VGG model, it shows that the VGG model seems to provide a reasonable estimate of $\text{Im}(H)$, possibly underestimated at the $\approx 20\%$ level. The parameter $a(\text{Re}(H))$ has a strong tendency to rise with t and although the uncertainties are large, it seems to be significantly different from the VGG prediction and it can differ by up to a factor of 4.

We display in table 3 the VGG reference values which, by multiplying the $a()$ GPD multipliers and their associated errors of table 2, allow us to extract the measured values of the CFFs themselves. We plot in fig. 8 the measurements of the two multipliers $a(\text{Im}(H))$ and $a(\text{Re}(H))$ and the associated CFFs for the t values for which they have finite uncertainties. In this figure, we show three results for each t for $a(\text{Im}(H))$ and $\text{Im}(H)$. These correspond

to the fits with the domains of variations $\{-3, 3\}$, $\{-5, 5\}$ and $\{-7, 7\}$ from left to right, respectively. The stability of the central value as well as the moderate increase of the error bar with the increase of the limit of the domain previously mentioned can be observed. As deviations of CFF values by a factor 7 (or even 5) from VGG predictions are not easy to conceive, the uncertainties quoted in table 2 and displayed in fig. 8 are very conservative. They could be reduced if, based on some models or educated guesses, smaller limits could be set on the other CFFs.

One should also note from table 2 that all fits have a χ^2 close to 1 except for the bin at $t = -0.33 \text{ GeV}^2$. We remark that a problem with this same bin was also observed in ref. [35] where, in an analysis mainly devoted to the JLab Hall-B BSAs, the JLab Hall-A BSAs, *i.e.* $\frac{\Delta\sigma_{z0}}{1+\beta\cos\phi}$, were fitted by the phenomenological function $\frac{\alpha\sin\phi}{1+\beta\cos\phi}$ where the β coefficient was found to take a peculiar value for this particular t bin, in clear distinction from the surrounding t bins. Also, in the present analysis, although the results for $a(\text{Re}(E))$ and $a(\text{Re}(\tilde{H}))$ are not very meaningful because of their ∞ uncertainties, one can nevertheless clearly observe a discontinuity in their fitted values as they jump rather abruptly from a largely negative value at the three low t values to a largely positive value for the last t . Therefore, there definitely seems to be a change of behavior in the data at this large t bin. A bad χ^2 may be indicating that our theoretical modeling is not appropriate. We recall that our analysis has been carried out at the twist-2 handbag level and that this intriguing change might signal the rise of higher-twist corrections.

Let us also mention that still a few more pieces of information can be extracted from the values of table 2. For several t values, $a(\text{Re}(\tilde{E}))$ has finite uncertainties. Since these error bars are systematically over 100%, it makes the information difficult to use, but we can simply note that the value of 1, which corresponds to the VGG pion pole, is never excluded and that our original assumption to neglect $\text{Im}(\tilde{E})$ on this basis is therefore not ruled out. There are a few cases in table 2 where only one uncertainty (σ_{a0}^- in general) is finite, which still yields some information. In particular, $\text{Im}(\tilde{H})$ for all t 's has a reliable (lower) bound.

We have also tried to fit only the $\Delta\sigma_{z0}$ observables (*i.e.* without the simultaneous fit of σ) which would be sensitive only to $\text{Im}(H)$, $\text{Im}(E)$ and $\text{Im}(\tilde{H})$. In general, the fitted central values for these CFFs were unstable, unless we guided and constrained the fit by setting limits on the domain of variation of the parameters. In gen-

eral, we obtained values of $\text{Im}(H)$ about 30% higher than those quoted in table 2 but they corresponded to much larger values of $\text{Im}(\tilde{H})$, compared to those of table 2, which with its opposite sign would provide some compensation. This kind of unstability is not unexpected because fitting only one observable with three parameters is even less constraining than fitting two observables with seven parameters.

Finally, we tried to fit the numerous JLab Hall-B BSAs [14]. We found that without any guidance of the fit or any physics input, no fit stability and robustness could be reached. This could actually be anticipated from our studies in the previous section. However, as we saw with fig. 3, guiding the fit by setting the initial values in MINUIT to values close to the expected ones, which can be relatively safely done for $\text{Im}(H)$ following our results on the Hall-A data that we just presented, could tremendously enhance the fit efficiency and stability. We delay to a forthcoming publication the results of such guided or educated fits.

5 Conclusion

In summary, we have developed a fitter program to extract GPD information from various DVCS observables at QCD leading twist and leading order. We have gained confidence in the program by checking its reliability and efficiency on simulated, ideal or realistic, pseudo-data. We came to the conclusion that by fitting enough unpolarized, singly and doubly polarized observables, with realistic experimental error bars, the code was able to extract in most of the cases the seven CFFs considered in this work, even in a very blind framework where all parameters are left free and essentially unconstrained. Applying realistic and educated constraints, such as dispersion relations or model motivated ansatzes, can only reduce the number of independent parameters or limit the range of variation of certain parameters and therefore improve the efficiency and reliability of this fitter program.

We recall that most of the aforementioned observables will be available in the near future from various experiments at JLab in particular. If only some of these nine observables are available, we have demonstrated that valuable partial GPD information could still be extracted: in particular, with σ , $\Delta\sigma_{z0}$ and $\Delta\sigma_{0z}$, which are planned to be measured in the very near future, the $\text{Im}(H)$, $\text{Im}(E)$ and $\text{Im}(\tilde{H})$ CFFs could be very reliably be known. For the real-part CFFs, one can either measure the beam charge difference of cross-sections or double-polarization observables.

Finally, we have extracted from the JLab Hall-A data first numerical values with associated uncertainties for the H GPD combinations $H(\xi, \xi, t) - H(-\xi, \xi, t)$ and $P \int_0^1 dx [H(x, \xi, t) - H(-x, \xi, t)] C^+(x, \xi)$. The corresponding error bars are rather large because we are fitting more parameters than observables and no *a priori* knowledge of any CFFs has been assumed in this study. Ultimately, when enough observables are available, this should indeed

not be needed, and we can consider that we have placed ourselves in this long-term perspective. In a forthcoming article, we will discuss strategies to reduce these uncertainties on the present data if educated assumptions are made about the CFFs. This code is only the first step towards a general fitting procedure of DVCS data (and potentially, if data lend themselves to a GPD interpretation, of exclusive meson electroproduction). Numerous extensions of the code are possible, such as introducing QCD higher-twists and/or higher-order corrections, implementing dispersion relations, and so forth.

The author has benefitted from numerous discussions with many colleagues from JLab and from the French ‘‘Nucleon GDR’’ group, whose list would be too long to enumerate but to whom the author is very thankful. Very special thanks are given to P. Desesquelles, M. Garçon, K. Griffioen, C. Muñoz Camacho and M. Vanderhaeghen. This work was supported by the French Agence Nationale de la Recherche program BLAN07-2_191986.

References

1. D. Müller, D. Robaschik, B. Geyer, F.-M. Dittes, J. Horejsi, *Fortschr. Phys.* **42**, 101 (1994).
2. X. Ji, *Phys. Rev. Lett.* **78**, 610 (1997); *Phys. Rev. D* **55**, 7114 (1997).
3. A.V. Radyushkin, *Phys. Lett. B* **380**, 417 (1996); *Phys. Rev. D* **56**, 5524 (1997).
4. J.C. Collins, L. Frankfurt, M. Strikman, *Phys. Rev. D* **56**, 2982 (1997).
5. K. Goeke, M.V. Polyakov, M. Vanderhaeghen, *Prog. Part. Nucl. Phys.* **47**, 401 (2001).
6. M. Diehl, *Phys. Rep.* **388**, 41 (2003).
7. A.V. Belitsky, A.V. Radyushkin, *Phys. Rep.* **418**, 1 (2005).
8. A. Airapetian *et al.*, *Phys. Rev. Lett.* **87**, 182001 (2001).
9. S. Stepanyan *et al.*, *Phys. Rev. Lett.* **87**, 182002 (2001).
10. S. Chen *et al.*, *Phys. Rev. Lett.* **97**, 072002 (2006).
11. A. Airapetian *et al.*, arXiv:0802.2499 [hep-ex].
12. A. Airapetian *et al.*, *Phys. Rev. D* **75**, 011103 (2007).
13. C. Muñoz Camacho *et al.*, *Phys. Rev. Lett.* **97**, 262002 (2006).
14. F.-X. Girod *et al.*, *Phys. Rev. Lett.* **100**, 162002 (2008).
15. JLab approved experiment E-05-114: *Deeply Virtual Compton Scattering at 6 GeV with polarized target and polarized beam using the CLAS detector*, spokespersons: A. Biselli, L. Elhouadrhiri, K. Joo, S. Niccolai.
16. JLab (conditionally) approved experiment E-08-021: *Deeply Virtual Compton Scattering at 6 GeV with transversely polarized target using the CLAS detector*, spokespersons: H. Avakian, V. Burkert, M. Guidal, R. Kaiser, F. Sabatié.
17. JLab approved experiment E-07-007: *Complete separation of Deeply Virtual Photon and π^0 electroproduction observables of unpolarized protons*, spokespersons: C. Muñoz Camacho, J. Roche, C. Hyde-Wright, P.-Y. Bertin.
18. JLab approved experiment E-06-003: *Deeply Virtual Compton Scattering with CLAS at 6 GeV*, spokespersons: V. Burkert, L. Elhouadrhiri, M. Garçon, R. Niyazov, S. Stepanyan.

19. JLab approved experiment E-12-06-114: *Measurements of Electron-Helicity Dependent Cross Sections of Deeply Virtual Compton Scattering with CEBAF at 12 GeV*, spokespersons: C. Hyde-Wright, B. Michel, C. Munoz Camacho, J. Roche.
20. JLab approved experiment E-12-06-119: *Deeply Virtual Compton Scattering with CLAS at 11 GeV*, spokespersons: V. Burkert, L. Elouadrhiri, M. Garçon, M. Holtrop, D. Ireland, K. Joo, W. Kim, F. Sabatié.
21. A. Belitsky, D. Muller, A. Kirchner, Nucl. Phys. B **629**, 323 (2002).
22. M. Mazouz *et al.*, Phys. Rev. Lett. **99**, 242501 (2007).
23. M. Guidal, M. Vanderhaeghen, Phys. Rev. Lett. **90**, 012001 (2003).
24. A.V. Belitsky, D. Muller, Phys. Rev. Lett. **90**, 022001 (2003).
25. O.V. Teryaev, arXiv/0510031 hep-ph; I.V. Anikin, O.V. Teryaev, Phys. Rev. D **76**, 056007 (2007).
26. M. Diehl, D.Y. Ivanov, arXiv:0707.0351 hep-ph.
27. K. Kumericki, D. Muller, K. Passek-Kumericki, Nucl. Phys. B **794**, 244 (2008).
28. M. Polyakov, M. Vanderhaeghen, arXiv:0803.1271 [hep-ph].
29. M. Vanderhaeghen, P.A.M. Guichon, M. Guidal, Phys. Rev. D **60**, 094017 (1999).
30. M. Guidal, M.V. Polyakov, A.V. Radyushkin, M. Vanderhaeghen, Phys. Rev. D **72**, 054013 (2005).
31. F. James, MINUIT, D507, CERN (1978).
32. M. Polyakov, C. Weiss, Phys. Rev. D **60**, 114017 (1999).
33. D.S. Hwang, D. Muller, Phys. Lett. B **660**, 350 (2008).
34. N. Kivel, M.V. Polyakov, M. Vanderhaeghen, Phys. Rev. D **63**, 114014 (2001).
35. F.X. Girod, PhD Thesis, Université Louis Pasteur, Strasbourg, France (2006).